Proton pitch angle distributions in the Martian induced magnetosphere: A survey of Tianwen-1 Mars Ion and Neutral Particle Analyzer observations

TaiFeng Jin[1*], BinBin Ni[1,2], LingGao Kong[3,4,5,6], AiBing Zhang[3,4,5,6], Lei Li[3,7], Song Fu[1], Xing Cao[1], WenYa Li[3,7], BinBin Tang[3,7], LiangHai Xie[3,7], YiTeng Zhang[3,7], ShuYue Pang[1], XiaoTong Yun[1], HengLe Du[1], FuHao Qiao[3,6,7], LiMin Wang[3,6,7], and JiJie Ma[3,6,7]

[1]Department of Space Physics, School of Electronic Information, Wuhan University, Wuhan 430072, China;

[2]Chinese Academy of Sciences Center for Excellence in Comparative Planetology, Hefei 230026, China;

[3]National Space Science Center, Chinese Academy of Sciences, Beijing 100190, China;

[4]Beijing Key Laboratory of Space Environment Exploration, Beijing 100190, China;

[5]Key Laboratory of Science and Technology on Space Environment Situational Awareness, Chinese Academy of Sciences, Beijing 100190, China;

[6]University of Chinese Academy of Sciences, Beijing 100049, China;

[7]State Key Laboratory of Space Weather, Chinese Academy of Sciences, Beijing 100190, China

Key Points:
- Data from the Mars Ion and Neutral Particle Analyzer onboard Tianwen-1 were first used to study the ion pitch angle distributions in the Martian induced magnetosphere.
- The ion pitch angle showed dominance of the field-aligned distribution type, whereas a discrepancy in distribution types occurred on the nightside of Mars.
- Asymmetry of the occurrence rate possibly indicates that wave–particle interactions occur on the nightside of Mars.

Abstract: The pitch angle distributions of ions and electrons can be affected by various processes; thus, they can serve as an important indicator of the physical mechanisms driving the dynamics of space plasmas. From observations from the Mars Ion and Neutral Particle Analyzer onboard the Tianwen-1 orbiter, we calculated the pitch angle distributions of protons in the Martian induced magnetosphere by using information from the magnetohydrodynamically simulated magnetic field, and we statistically analyzed the spatial occurrence pattern of different types of pitch angle distributions. Even though no symmetrical features were seen in the dataset, we found the dominance of the field-aligned distribution type over the energy range from 188 to 6232 eV. Maps of the occurrence rate showed the preferential presence of a trapped-like distribution at the lower altitudes of the surveyed nightside region. Although our results are more or less restricted by the adopted magnetic field, they indicate the complexity of the near-Mars proton pitch angle distributions and infer the possibility of wave–particle interactions in the Martian induced magnetosphere.

Keywords: Martian plasma environment; ion pitch angle distribution; Tianwen-1 Mars Ion and Neutral Particle Analyzer (MINPA)

1. Introduction

The dynamics of particles in the magnetosphere has long been a major topic in space plasma physics. The free energy carried by the plasma can trigger various kinds of instabilities to form waves and other dissipation structures. Meanwhile, waves interact with particles to cause their acceleration and loss processes. The pitch angle is a fundamental parameter describing the features and behavior of particles. The processes of ion acceleration, transport, and loss are usually indicated by the ion pitch angle distribution and its associated variations. For example, inside the radiation belt of Earth, the butterfly-like pitch angle distribution of electrons is considered to be related to the drift shell splitting and the magnetopause shadowing effect (e.g., Selesnick and Blake, 2002), and its occurrence rate is affected by the magnetic local time and the solar wind dynamic pressure (Ni BB et al., 2016). Hiss, chorus, and electromagnetic ion cyclotron (EMIC) waves are responsible for the observed top-flat distributions of electrons by scattering those with pitch angles near 90° to lower angles (e.g., Albert, 2003; Zhu H et al., 2020). The pitch angle scattering combined

with the adiabatic focusing effect is considered to affect the dynamics of energetic ions in the interplanetary medium during solar energetic particle events.

Without an intrinsic global magnetic field, Mars has its ionosphere, formed by the photoionization of the upper atmosphere, as an obstacle of the supersonic solar wind by the induced magnetic field within. A bow shock is thus formed, downstream of which the decelerated solar wind carries the frozen-in magnetic field, the latter draped and piled up at the surface of the dayside ionosphere to form the magnetic pile-up region (MPR) resembling the magnetosphere of Earth and Jupiter (e.g., Nagy et al., 2004). The upper boundary of the MPR, called the magnetic pile-up boundary (MPB), separates the MPR from the magnetosheath, which is located between the MPB and the bow shock. The average altitudes of the bow shock and the MPB at the subsolar point are 0.58 R_M and 0.33 R_M, respectively (where R_M is the Martian radius, and 1 R_M = 3389.5 km; Edberg et al., 2008), indicating a highly restricted spatial scale compared with that of Earth. At the same time, the altitudes of the boundaries are affected by the irregularly distributed crustal field to possess a north–south asymmetry (Matsunaga et al., 2017). All factors combine to form a plasma environment of the Martian magnetosphere quite different from that of Earth (e.g., Halekas et al., 2017). In addition, the crustal field of Mars can further affect the interaction between the planet and the solar wind. Ma YJ et al. (2014) found, using magnetohydrodynamic (MHD) simulation results combined with observations of the Mars Global Surveyor, that the ion escape rate at Mars is modulated by the self-rotation of the planet and is roughly anti-correlated with the strength of the crustal field at the subsolar point.

Studies of the pitch angle distribution of particles in the Martian magnetosphere have thus far been focused mainly on the photo-electrons. Because the electrons travel along the magnetic field lines, the pitch angle distribution of electrons can be used to deduce the topology of the magnetic field lines (Weber et al., 2017). Xu SS et al. (2019) used the technique described above to combine the energy distribution of suprathermal electrons. They found several types of closed magnetic field line structures inside the Martian ionosphere at the dawn–dusk plane connecting different regions of the crustal field on the surface of Mars. By comparing the electron pitch angle distributions in the dayside and nightside ionosphere of Mars, Cao YT et al. (2020) found that photoelectrons are transported from the dayside to the nightside through magnetic lines. Studies of protons are much more limited. Wang J et al. (2020) used Mars Atmosphere and Volatile Evolution (MAVEN) observations to reveal the north–south asymmetry of proton density in the Martian magnetosheath, which is likely related to the distribution of the Martian crustal field.

Limited studies have thus far implied the necessity of further investigations of the distribution of the proton pitch angle at Mars. In this work, we aimed to present the statistical feature of the pitch angle distribution of protons in the Martian induced magnetosphere by using Mars Ion and Neutral Particle Analyzer (MINPA) observations with a magnetic field obtained from a global MHD simulation. We describe the instrument and the data and calculation methods used in this study in Section 2. The results are shown in Section 3. Section 4 summarizes the study, along with a brief discussion.

2. Instrument and Data Description

2.1 Instrument and Data Product

Data from the MINPA onboard the Tianwen-1 orbiter were used in this study. Tianwen-1 was launched on July 23, 2020, and entered the Mars orbit successfully on February 10, 2021. After serving as a telecommunication relay for the Zhurong rover, the orbiter began its scientific detection phase in November 2021, following an elliptic orbit with its apoapsis and periapsis points at 12,000 km and 265 km, respectively, and an inclination of 93°, covering the Martian space ranging from upstream to the magnetotail. The MINPA instrument was designed to detect ions and energetic neutral atoms of multiple species, with a time resolution of ion detection up to 4 s, and an angular resolution of 22.5° × 5.625° covering a 2π field of view (Kong LG et al., 2020).

Hydrogen ion (H$^+$) data from the MOD-01 package were used for this study and were processed to remove noise signals in azimuthal channels. Because the magnetic field data from the Mars Orbiter Magnetometer (MoMAG, the magnetometer onboard the Tianwen-1 orbiter) are not yet publicly available, we adopted the simulated magnetic field from an MHD model (Ma YJ et al., 2004) in this study to calculate the pitch angle of protons. The particle density and the velocity of the solar wind were set to 2.5 cm^{-3} and 400 km/s, respectively, as upstream conditions of the simulation, together with the upstream interplanetary magnetic field B = (−1.67, 2.49, 0.0) nT and the solar wind temperature $T = 3.5 \times 10^5$ K. The Martian crustal field model was also adopted, with the strongest anomaly located at noon.

The region downstream of the bow shock was exclusively selected by checking the solar inclined angle (SIA), solar azimuthal angle (SAA), and MHD B values. The SIA and SAA are measured independently from the spacecraft attitude module, thus providing the reference of the instrument frame, definitions of which are given in Kong LG et al. (2020). Because the upstream region shares a unique magnetic field value in the simulation, the downstream region can be selected by searching for variations in the magnetic field value along the trajectory of the spacecraft. In addition, because information on the satellite attitude is incomplete, all data points corresponding to discontinuous SIA and SAA values were removed to obtain convincing results of the pitch angle calculation.

2.2 Energy Range Coverage of Differential Flux Data Validity

We summed the flux value in each energy channel to check the validity of the signal. As shown in Figure 1, only channels 19–34 and channel 14 received a nonzero signal. Channels 19–34 cover the energy range from 188 to 6232 eV, whereas channel 14 corresponds to the energy range centered at 58 eV. The gap between channel 14 and channel 19 is presumably due to the cut-off caused by the MINPA instrument itself. We selected the data from channels 19–34, which contain the majority of the valid signals, for further analysis.

2.3 Quantification Method for the Pitch Angle Distribution Analysis

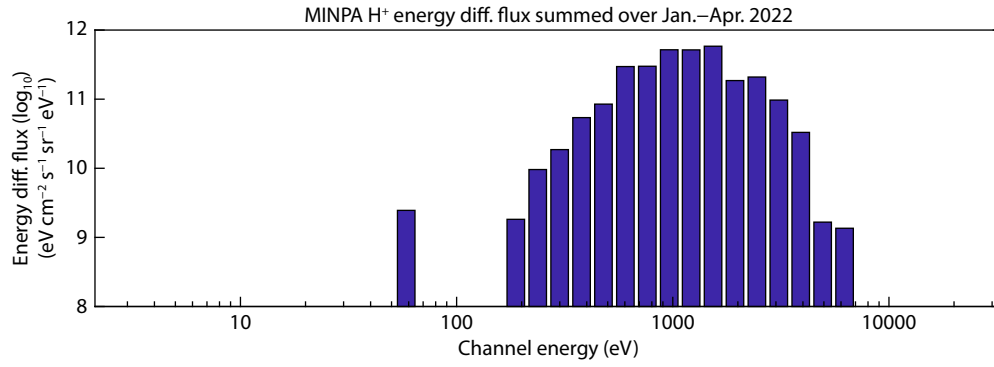Before calculating the pitch angle, we divided the selected chan-

Figure 1. Hydrogen ion (H⁺) omni-differential energy flux distribution along energy channels. MINPA, Mars Ion and Neutral Particle Analyzer.

nels into three subgroups to compare the features of particles above and below the typical solar wind energy. The energy (E) range of each group was selected as follows: the low range, covering $E < 683$ eV; the mid range, covering 683 eV $< E < 1.74$ keV; and the high range, covering $E < 1.74$ keV. The mid range included protons with energy comparable to that of the solar wind; hence, the low range and the high range represented decelerated and accelerated (i.e., energetic) protons, respectively. The differential flux was then converted into the phase space density (PSD) for pitch angle calculations. Because protons are much heavier than electrons, the bulk velocity of protons should be removed from the distribution (i.e., Gomez et al., 2019; Kim et al., 2022).

After calculating the pitch angle, we analyzed two aspects of its distribution, the symmetry and the anisotropy. The range of the pitch angle (0°–180°) was evenly divided into 6 bins as the first step of quantification. For clarity, the bins were labeled from 1 to 6, where bin 1 corresponded to the pitch angle range from 0° to 30° and bin 6 corresponded to the range from 150° to 180°. The average PSD in each bin F_i was then calculated, with the subindex i denoting the bin number. It was obvious that bin 1 and bin 6, bin 2 and bin 5, and bin 3 and bin 4 were symmetrical along 90°.

2.3.1 Symmetry

In this study, the symmetry of the pitch angle distribution is defined as follows: a distribution is considered symmetrical only when the PSD of symmetrical bins differs by less than 10%. More specifically, a symmetrical distribution satisfies the following criteria:

$$(1 - 10\%)F_6 \leq F_1 \leq (1 + 10\%)F_6, \tag{1}$$

$$(1 - 10\%)F_5 \leq F_2 \leq (1 + 10\%)F_5, \tag{2}$$

$$(1 - 10\%)F_4 \leq F_3 \leq (1 + 10\%)F_4. \tag{3}$$

Otherwise, the distribution is considered asymmetrical.

2.3.2 Anisotropy

The definition of anisotropy of distribution was adapted from that of Motoba et al. (2020). The perpendicular PSD is defined as

$$F_\perp = F_3 + F_4, \tag{4}$$

and the parallel PSD is defined as

$$F_{//} = F_1 + F_6. \tag{5}$$

The anisotropy of distribution, A, is then calculated as

$$A = \begin{cases} F_\perp/F_{//} - 1, & \text{when } F_\perp > F_{//} \\ -F_{//}/F_\perp + 1, & \text{when } F_\perp < F_{//} \end{cases}. \tag{6}$$

The distribution is considered isotropic when $|A| < 0.5$. When $A < -0.5$, it indicates a distribution showing anisotropy in parallel directions (i.e., field-aligned distribution), whereas $A > 0.5$ indicates a perpendicularly anisotropic distribution (i.e., trapped-like distribution). The terms "field-aligned" distribution and "trapped-like" distribution are used indiscriminately in the rest of this article to refer to distributions with anisotropy in a parallel or perpendicular direction. An example of the three types of distribution is shown in Figure 2. The blue line shows a field-aligned distribution ($A = -1.98$), the red line shows a trapped-like distribution ($A = 2.83$), and the yellow line shows an isotropic distribution ($A = 0.18$).
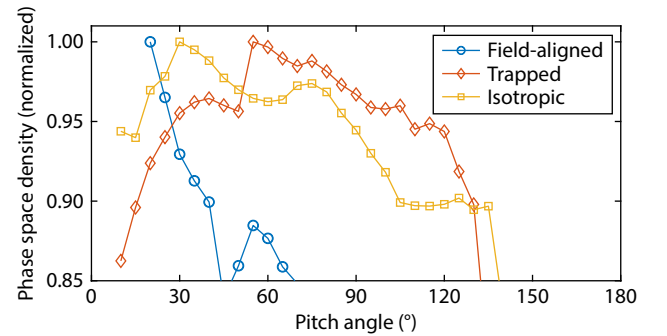

Figure 2. Example of the three types of distribution. The blue line with circles shows a field-aligned distribution, sampled on January 16, 2022, at 22:28, $A = -1.98$; the red line with diamonds shows a trapped-like distribution, sampled on January 23, 2022, at 05:10, $A = 2.83$; and the orange line with squares shows an isotropic distribution, sampled on January 23, 2022, at 05:11, $A = 0.18$.

3. Statistical Results

Data from January to April of 2022 were investigated, from which valid sampling points were selected and analyzed by using the methods described above. No symmetrical distribution was seen in the entire dataset. We attributed this result partially to the static magnetic field used in calculating the pitch angle, which cannot fully reveal the interaction of particles and field; in addition, the much greater mass of protons compared with electrons likely limited their response during energy exchange with varying fields.

3.1 Spatial Coverage of the Dataset Used

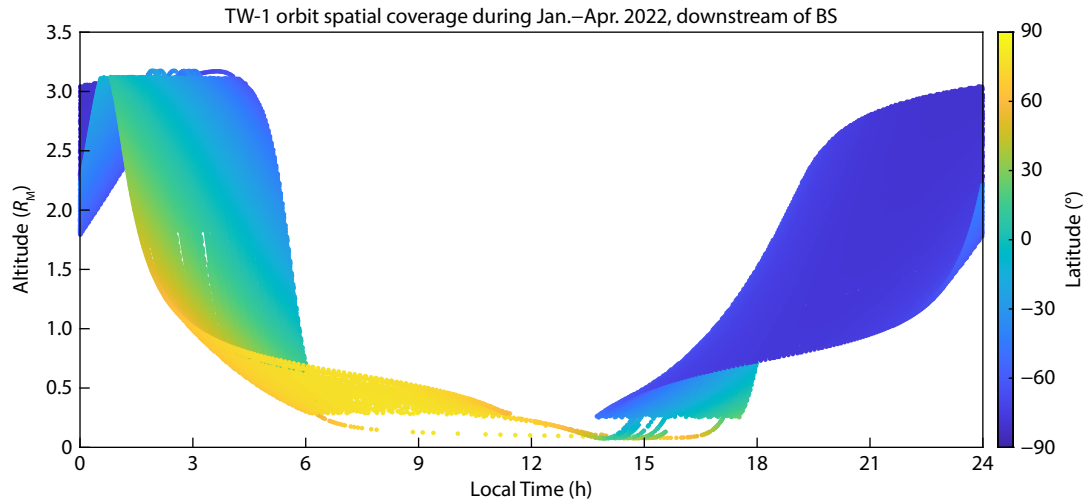Figure 3 presents the spatial coverage of selected data points,

Figure 3.   Spatial coverage of the investigated dataset. TW-1, Tianwen-1; BS, bow shock.

from which the asymmetry in the spatial distribution of orbit coverage can clearly be seen. The orbit at dayside is always lower than 1 R_M, whereas at nightside, the orbiter covers a wide range of altitude from ~0.5 R_M to higher than 3 R_M. In addition, the latitude distribution shows clear dawn–dusk asymmetry. At the dawn side, the orbiter mainly covers the northern hemisphere from the equator to a high latitude, whereas at the dusk side, the orbiter travels almost exclusively in the high-latitude region of the southern hemisphere.

3.2 Energy Dependence of Anisotropy

Figure 4 shows the energy dependence of anisotropy of the H$^+$ pitch angle distribution. The length of each colored section refers to the occurrence ratio (normalized by total valid sampling points in each energy group) of the corresponding distribution type. The field-aligned distribution is dominant (nearly 50%) throughout the selected energy range and possesses a higher percentage at
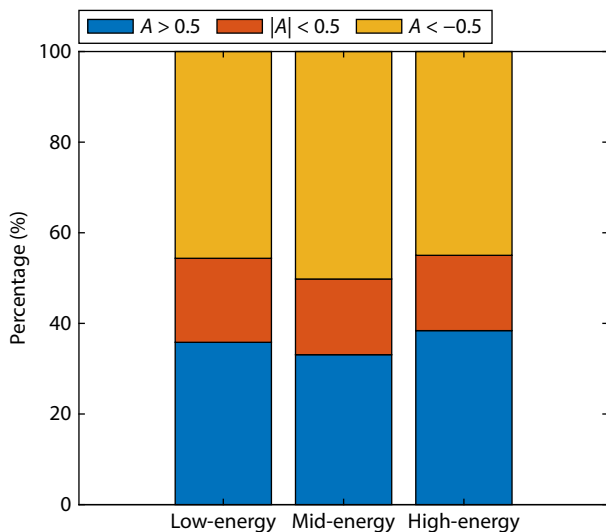

Figure 4.   Energy dependence of the distribution anisotropy. The colors indicate different types of distributions: blue for a trapped-like distribution, red for an anisotropic distribution, and orange for a field-aligned distribution.

the mid-energy range. The ratio of the perpendicularly anisotropic distribution peaks at the high-energy range, reaching 38.40%, but it remains greater than 30% in the other two groups. Isotropic distributions never exceed 20% in the entire energy range selected, thus showing the least possibility of occurring.

3.3 Spatial Distribution of Anisotropy

Next, we considered the spatial distribution of anisotropy along the altitude and local time (longitude). To analyze the spatial distribution, the Martian space was divided into bins of 1 hour × 0.5 R_M, and the data points in each bin were added. The distribution information along the latitudes was thus not analyzed; however, considering that the orbital coverage showed clear asymmetry in the latitudes, we believe the quantification above had little effect on the result. The number of total data points in each bin, $N(i, j)$ (where i and j denote the index of local time and the altitude bin, respectively), and samples with the pitch angle distribution showing the feature of perpendicular anisotropy ($N_{trap}(i, j)$), field-aligned anisotropy ($N_{fa}(i, j)$), and isotropy ($N_{iso}(i, j)$), were counted to calculate the occurrence ratio R of each type of distribution, defined as $R_{fa} = N_{fa}(i, j)/N(i, j)$, $R_{iso} = N_{iso}(i, j)/N(i, j)$, $R_{trap} = N_{trap}(i, j)/N(i, j)$. Figure 5 shows the spatial distribution of valid samples ($N(i, j)$) used in our statistical analysis. Bins with sample points less than 100 were neglected because insufficient samples would affect the reliability of the statistical results. Readers are encouraged to compare this figure with Figure 3 for better understanding. The sample distribution shows an obvious concentration in the 01:00–05:00 local time (LT) sectors at the high-altitude range, where the apoapsis of the Tianwen-1 orbiter occurred during the selected period of time. The rest of the distribution is rather even, with slightly more samples concentrated at mid-altitude on the dusk side, especially in the 17:00–19:00 LT sectors.

The plots in Figure 6, divided by the energy ranges of interest from low to high, map the occurrence rates of field-aligned, isotropic, and trapped-like distributions, with respect to the time sector and altitude. Generally, as can also be seen from Figure 4, the field-aligned distributions (Figures 6a, 6d, and 6g) occur more frequently than the other two types in most of the surveyed area
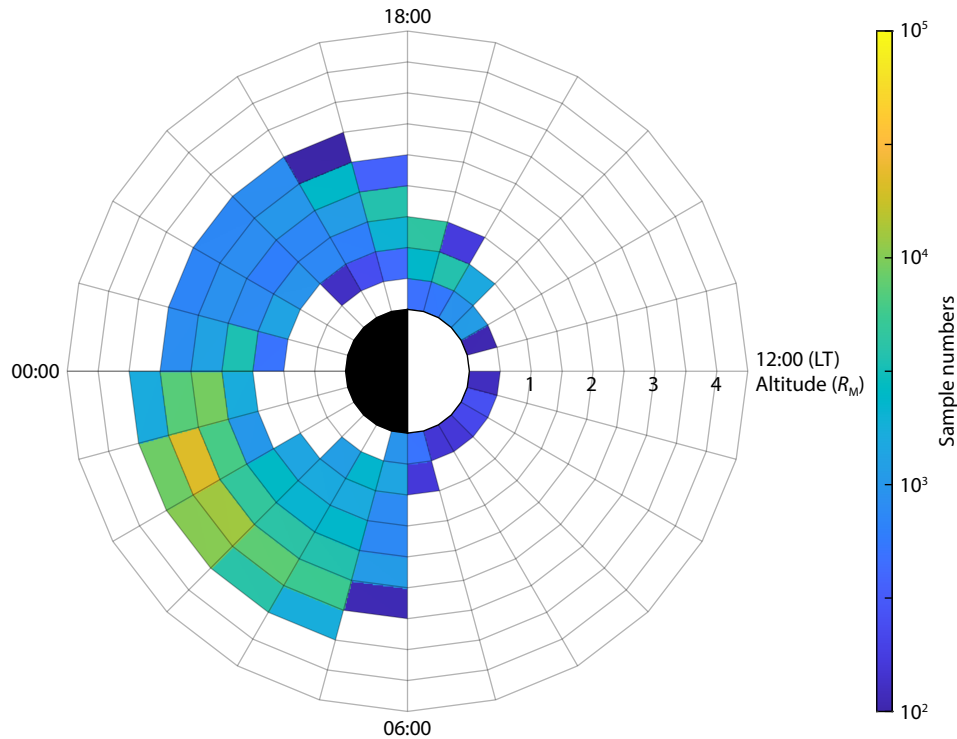
Figure 5. Local time and altitude distribution of all the samples. The radii of co-centered circles represent the altitude, increasing radially at a step of 0.5 R_M, whereas the radial lines divide the space into 1-hour time sectors. The numbers assigned denote the local time. The horizontal line denotes the direction of the x-axis in the Mars Solar Orbital frame. The sun is located to the right of Mars.

for all energy ranges, except for the high-energy group in the 18:00–24:00 LT sectors and for the low-energy group in the 01:00–06:00 LT sectors, both at a lower altitude region. The isotropic distributions (Figures 6b, 6e, and 6h), on the other hand, show lower occurrence rates in general, except for the mid-energy range in the 01:00–05:00 LT sectors, the occurrence of which is comparable to the other two types of distribution.

The dayside is generally dominated by anisotropic distributions. In the 06:00–12:00 LT sectors, the spacecraft surveyed at a low altitude (<1 R_M) in the high-latitude region of the northern hemisphere. The trapped-like type was more frequently seen for mid- and high-energy group protons (especially at a higher altitude), whereas the low-energy group protons tended to be field aligned. As for the 12:00–18:00 LT sectors, the high-energy protons tended to be more trapped-like at a higher altitude and more field-aligned at a lower altitude, whereas the mid- and low-energy protons showed opposite features, being more trapped-like at a low altitude and more field-aligned at a higher altitude. The trapped-like distributions for mid- and low-energy protons closely resemble each other.

The nightside, owing to the richer dataset of observations, exhibited clearer features and dependencies in distributions of different types of pitch angle distributions; nevertheless, the field-aligned type showed dominance at the >2 R_M altitude region regardless of the energy range. In the 00:00–06:00 LT sectors, a rather clear boundary located at ~2 R_M could be seen in the map of field-aligned distributions of the low-energy range protons. The altitude of the boundary diminished toward the dawn–dusk plane to ~1.5 R_M and increased toward the meridional line to ~2.5 R_M, the

variation of which resembled the shape of the MPB in the nominal condition. The same distinguishing characteristic was also obvious in maps of trapped-like distributions, only with the occurrence rates inverted in two altitude regions. It is interesting that for high-energy protons, the distribution feature of the occurrence rate of anisotropic pitch angle distributions below ~2 R_M in the same local time zone appeared opposite, preferring field-aligned distributions at a lower altitude and the opposite for trapped-like distributions. At the same time, the occurrence rates of both distribution types remained comparable with that for low-energy range protons.

The 18:00–24:00 LT sectors also exhibited a boundary at ~2 R_M, the occurrence rates of field-aligned and trapped-like distributions above and below which showed the opposite trend, as most clearly seen in the distributions of high-energy protons. Below the boundary, the field-aligned distribution was less likely to occur compared with the trapped-like distribution. The contrast in the occurrence rate of distributions in the two altitude regions was not as sharp as that in the 00:00–06:00 LT sectors, showing instead a rather gradual transition across the boundary. The occurrence rates of the field-aligned distribution also differed between high-energy and low-energy protons (e.g., compare Figures 6a and 6g), although the trend for low-energy protons was not as obvious as that for high-energy ones. When the subplots in Figure 6 are compared diagonally, one can see the similarity between the trapped-like distribution of high-energy protons and the field-aligned distribution of low-energy protons (Figures 6c and 6g), as well as that between field-aligned high-energy protons and trapped-like low-energy protons (Figures 6a and 6i), especially in
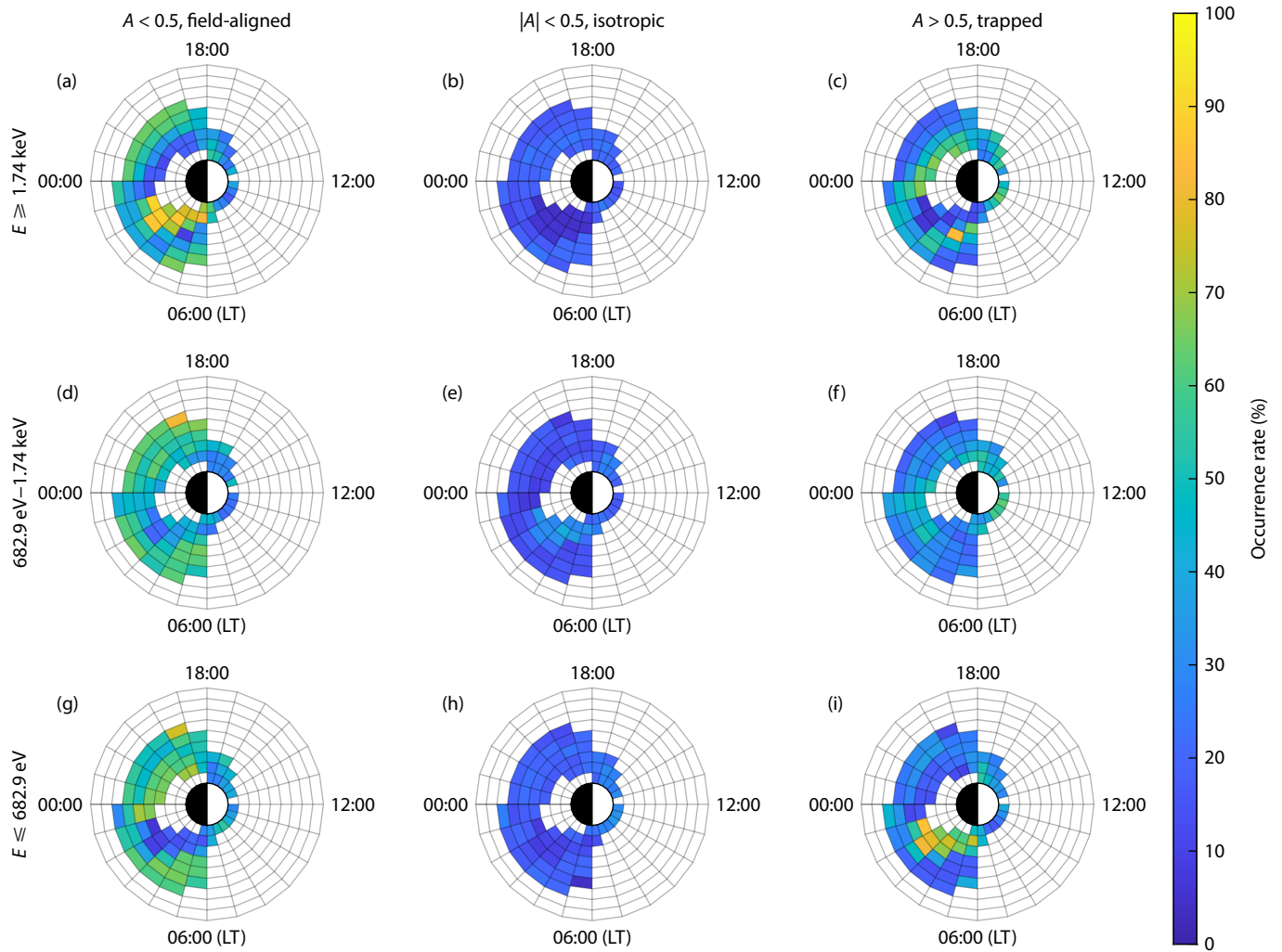
Figure 6. Occurrence rates of hydrogen ion (H⁺) distribution anisotropy for the three energy groups. Each subplot shares the same format as Figure 5, with the color in each bin indicating the average occurrence rate of the distribution of the given type.

the altitude region below ~2 R_M. In other words, the trapped-like high-energy protons behave similarly to the field-aligned low-energy protons, whereas the field-aligned high-energy protons resemble the trapped-like low-energy protons.

4. Conclusions and Discussion

In this study, we calculated and statistically analyzed the pitch angle distributions of H⁺ by using the observational data from MINPA onboard the Tianwen-1, based on the MHD-simulated Martian magnetic field. In the selected dataset from January to April of 2022, the distributions tended to be predominantly field-aligned, and no symmetrical features were found within. Statistical analysis of the spatial distribution of the occurrence rates of different types of proton pitch angle distributions revealed a discrepancy between the two hemispheres on the nightside of Mars in the lower altitude region, as well as between different energy ranges of H⁺. Although the field-aligned distributions were preferred in both hemispheres at higher altitudes, at lower altitudes, high-energy protons preferred the field-aligned distributions over the trapped-like ones, and low-energy protons showed exactly the opposite feature, being trapped like more frequently than field-

aligned. A clear boundary appeared in the maps of the field-aligned and trapped-like distributions of low-energy protons. Compared with Figure 3, one can see that the spacecraft traveled near the equatorial plane at corresponding altitudes, which implies a relationship exists between the boundary and the plasma flow in the Martian magnetosheath because the boundary is close to the nominal location of the MPB.

The discrepancy in the distribution occurrence between the two hemispheres is unlikely to have been caused by the crustal field of Mars, which is mainly distributed in the southern hemisphere. On one hand, the altitudes at which the discrepancy appears exceed the spatial range affected by the crustal field. On the other hand, the crustal field model used for our MHD simulations sets the magnetic anomaly to be located at noon. Alternatively, the wave–particle interaction is one possibility capable of producing such distributions of ions. Electron cyclotron harmonic waves, in terms of resonant diffusion, can lead to a "pancake-like" (trapped-like) distribution (Horne and Thorne, 2000). Resonant scattering by EMIC waves is thought to be responsible for ion heating at the terrestrial plasmasphere (Ma Q et al., 2019). Magnetosonic waves are also capable of heating protons and altering the pitch angle

distribution to be more trapped like (Yuan ZG et al., 2018; Teng S et al., 2019). However, the energy range of protons affected by such waves, usually not greater than several hundreds of electrovolts, is rather low compared with the ion population in this study. Future investigations are expected using forthcoming magnetic field data from the Tianwen-1 MoMAG or measurements from MAVEN, not only for better accuracy in the magnetic field, but also for examining wave structures so that the underlying correlation between the proton pitch angle distributions and wave–particle interactions on Mars can be better understood.

Acknowledgments

References

Albert, J. M. (2003). Evaluation of quasi-linear diffusion coefficients for EMIC waves in a multispecies plasma. *J. Geophys. Res.: Space Phys.*, *108*(A6), 1249. https://doi.org/10.1029/2002JA009792

Cao, Y. T., Cui, J., Wu, X. S., and Zhong, J. H. (2020). Photoelectron pitch angle distribution near Mars and implications on cross terminator magnetic field connectivity. *Earth Planet. Phys.*, *4*(1), 17–22. https://doi.org/10.26464/epp2020008

Edberg, N. J. T., Lester, M., Cowley, S. W. H., and Eriksson, A. I. (2008). Statistical analysis of the location of the Martian magnetic pileup boundary and bow shock and the influence of crustal magnetic fields. *J. Geophys. Res.: Space Phys.*, *113*(A8), A08206. https://doi.org/10.1029/2008JA013096

Gomez, R. G., Fuselier, S. A., Mukherjee, J., Gonzalez, C. A., Burch, J. L., Strangeway, R. J., and Starkey, M. J. (2019). The extra-magnetospheric ion environment as observed by the Magnetospheric Multiscale mission hot plasma composition analyzer (MMS-HPCA). *J. Geophys. Res.: Space Phys.*, *124*(3), 1509–1524. https://doi.org/10.1029/2018JA025392

Halekas, J. S., Brain, D. A., Luhmann, J. G., DiBraccio, G. A., Ruhunusiri, S., Harada, Y., Fowler, C. M., Mitchell, D. L., Connerney, J. E. P., … Jakosky, B. M. (2017). Flows, fields, and forces in the Mars–solar wind interaction. *J. Geophys. Res.: Space Phys.*, *122*(11), 11320–11341. https://doi.org/10.1002/2017JA024772

Horne, R. B., and Thorne, R. M. (2000). Electron pitch angle diffusion by electrostatic electron cyclotron harmonic waves: The origin of pancake distributions. *J. Geophys. Res.: Space Phys.*, *105*(A3), 5391–5402. https://doi.org/10.1029/1999JA900447

Kim, M. J., Goldstein, J., Fuselier, S. A., and Burch, J. L. (2022). H^+ pitch angle distributions in the outer magnetosphere observed by MMS HPCA. *J. Geophys. Res.: Space Phys.*, *127*(4), e2021JA029648. https://doi.org/10.1029/2021JA029648

Kong, L. G., Zhang, A. B., Tian, Z., Zheng, X. Z., Wang, W. J., Liu, B., Wurz, P., Piazza, D., Etter, A., … Sun Y. Q. (2020). Mars Ion and Neutral Particle Analyzer (MINPA) for Chinese Mars Exploration Mission (Tianwen-1): Design

and ground calibration. *Earth Planet. Phys.*, *4*(4), 333–344. https://doi.org/10.26464/epp2020053

Ma, Q., Li, W., Yue, C., Thorne, R. M., Bortnik, J., Kletzing, C. A., Kurth, W. S., Hospodarsky, G. B., Reeves, G. D., and Spence, H. E. (2019). Ion heating by electromagnetic ion cyclotron waves and magnetosonic waves in the Earth's inner magnetosphere. *Geophys. Res. Lett.*, *46*(12), 6258–6267. https://doi.org/10.1029/2019GL083513

Ma, Y. J., Nagy, A. F., Sokolov, I. V., and Hansen, K. C. (2004). Three-dimensional, multispecies, high spatial resolution MHD studies of the solar wind interaction with Mars. *J. Geophys. Res.: Space Phys.*, *109*(A7), A07211. https://doi.org/10.1029/2003JA010367

Ma, Y. J., Fang, X. H., Russell, C. T., Nagy, A. F., Toth, G., Luhmann, J. G., Brain, D. A., and Dong, C. F. (2014). Effects of crustal field rotation on the solar wind plasma interaction with Mars. *Geophys. Res. Lett.*, *41*(19), 6563–6569. https://doi.org/10.1002/2014GL060785

Matsunaga, K., Seki, K., Brain, D. A., Hara, T., Masunaga, K., Mcfadden, J. P., Halekas, J. S., Mitchell, D. L., Mazelle, C., … Jakosky, B. M. (2017). Statistical study of relations between the induced magnetosphere, ion composition, and pressure balance boundaries around Mars based on MAVEN observations. *J. Geophys. Res.: Space Phys.*, *122*(9), 9723–9737. https://doi.org/10.1002/2017JA024217

Motoba, T., Ohtani, S., Gkioulidou, M., Mitchell, D. G., Ukhorskiy, A. Y., Takahashi, K., Lanzerotti, L. J., Claudepierre, S. G., Spence, H. E., and Reeves, G. D. (2020). Pitch angle dependence of electron and ion flux changes during local magnetic dipolarization inside geosynchronous orbit. *J. Geophys. Res.: Space Phys.*, *125*(2), e2019JA027543. https://doi.org/10.1029/2019JA027543

Nagy, A. F., Winterhalter, D., Sauer, K., Cravens, T. E., Brecht, S., Mazelle, C., Crider, D., Kallio, E., Zakharov, A., … Trotignon, J. G. (2004). The plasma environment of Mars. *Space Sci. Rev.*, *111*(1–2), 33–114. https://doi.org/10.1023/B:SPAC.0000032718.47512.92

Ni, B. B., Zou, Z. Y., Li, X. L., Bortnik, J., Xie, L., and Gu, X. D. (2016). Occurrence characteristics of outer zone relativistic electron butterfly distribution: A survey of Van Allen Probes REPT measurements. *Geophys. Res. Lett.*, *43*(11), 5644–5652. https://doi.org/10.1002/2016GL069350

Selesnick, R. S., and Blake, J. B. (2002). Relativistic electron drift shell splitting. *J. Geophys. Res.: Space Phys.*, *107*(A9), 1265. https://doi.org/10.1029/2001JA009179

Teng, S., Li, W., Tao, X., Ma, Q., Wu, Y., Capannolo, L., Shen, X. C., and Gan, L. (2019). Generation and characteristics of unusual high frequency EMIC waves. *Geophys. Res. Lett.*, *46*(24), 14230–14238. https://doi.org/10.1029/2019GL085220

Wang, J., Xu, X. J., Yu, J., and Ye, Y. D. (2020). South–north asymmetry of proton density distribution in the Martian magnetosheath. *Earth Planet. Phys.*, *4*(1), 32–37. https://doi.org/10.26464/epp2020003

Weber, T., Brain, D., Mitchell, D., Xu, S. S., Connerney, J., and Halekas, J. (2017). Characterization of low-altitude nightside Martian magnetic topology using electron pitch angle distributions. *J. Geophys. Res.: Space Phys.*, *122*(10), 9777–9789. https://doi.org/10.1002/2017JA024491

Xu, S. S., Weber, T., Mitchell, D. L., Brain, D. A., Mazelle, C., DiBraccio, G. A., and Espley, J. (2019). A technique to infer magnetic topology at Mars and its application to the terminator region. *J. Geophys. Res.: Space Phys.*, *124*(3), 1823–1842. https://doi.org/10.1029/2018JA026366

Yuan, Z. G., Yu, X. D., Huang, S. Y., Qiao, Z., Yao, F., and Funsten, H. O. (2018). Cold ion heating by magnetosonic waves in a density cavity of the plasmasphere. *J. Geophys. Res.: Space Phys.*, *123*(2), 1242–1250. https://doi.org/10.1002/2017JA024919

Zhu, H., Chen, L. J., Claudepierre, S. G., and Zheng, L. H. (2020). Direct evidence of the pitch angle scattering of relativistic electrons induced by EMIC waves. *Geophys. Res. Lett.*, *47*(4), e2019GL085637. https://doi.org/10.1029/2019GL085637